Supporting Information

Progressive nucleation mechanism enables stable zinc stripping-plating behavior

Yihu Li, Pengfei Wu, Wei Zhong, Chunlin Xie, Yanling Xie, Qi Zhang, Dan Sun, Yougen Tang, Haiyan Wang**

[a] *Hunan Provincial Key Laboratory of Chemical Power Sources, College of Chemistry and Chemical Engineering, Central South University, Changsha 410083 (China). E-mail: sundan4330@csu.edu.cn; wanghy419@csu.edu.cn*

Experimental section

Characterizations: The X-ray Photoelectron Spectroscopy (XPS) was conducted by the Axis Ultra DLD Kratos AXIS SUPRA. The X-ray diffraction (XRD) patterns were recorded using a Bruker D8 X-ray diffractometer with monochromatized Cu Kα radiation (wavelength = 1.5406 Å). The morphologies of zinc deposition on zinc foils were characterized by scanning electron microscopy (SEM, Quanta FEG 250 and JSM-7610FPlus.), and those zinc foils were stripped for 12 min at 5 $mA \cdot cm^{-2}$ before plating. All of the tested samples for XPS, XRD and SEM were prepared by means of the membrane-free device shown in Figure S19 which consists of three acrylic plates, which are marked as A, B and C. Two pieces of zinc foils are sandwiched between A and B and between C and B, respectively. The electrolyte is stored in the hole centering at B to connect A and C. Before tests, they were washed by deionized water and alcohol for cleaning. The in-situ optical microscopic observations of zinc deposition were performed in a self-made cell. The CHI660e electrochemical workstation (Shanghai Chenhua, China) was adopted to apply a constant current (5.0 $mA \cdot cm^{-2}$). Images and videos were collected by the Stereo Microscope Optics (Nikon SMZ25).

Materials synthesis: Commercial V_2O_5 powder (3.0 g, Alfa Aesar) was added into a NaCl aqueous solution (2 $mol \cdot L^{-1}$). After stirring at 30 °C for 72 h in a water bath, the suspension was centrifuged and washed with deionized water and ethanol several times. Finally, the $NaV_3O_8 \cdot 1.5H_2O$ nanowires were collected by freeze-drying.[1]

Assembly of symmetric cells: All reagents were used as supplied without further modification. First, the as-received glass fiber was punched into circles in a diameter of 18 mm. Then CR2025 coin-type symmetric cells were assembled with the glass fiber circles as separators, two identical zinc foils discs (1.2 cm in diameter, 0.03 mm in thickness) as the cathode and anode. The aqueous $ZnSO_4$ solution (1 $mol \cdot L^{-1}$) was taken as the normal electrolyte, and different amounts of $Ce_2(SO_4)_3$ or $La_2(SO_4)_3$ were added as the electrolyte additive. After resting for 4 h to achieve a steady state, the coin cells were ready for further electrochemical tests.

Assembly of full cells: A homogeneous slurry was obtained by grinding the as-synthesized $NaV_3O_8 \cdot 1.5H_2O$ nanowires (70 wt%), super P carbon (20 wt%), and Polytetrafluoroethylene (PTFE) (10 wt%). Then, the resulting slurry was ground until they can be rolled onto stainless steel (SS) mesh (Φ12 mm), and dried in vacuum at 80 °C overnight. The CR2025-type coin cells were fabricated in ambient conditions using zinc foil (Φ = 16 mm) as the anode. 1M $ZnSO_4$ solution as the normal electrolyte and 0.01 M $Ce_2(SO_4)_3$ was added as the electrolyte additive. Commercial

glass fiber was used as separators. The assembled cells were rested for 8 h before electrochemical tests.

Electrochemical measurements: Quartz Crystal Microbalance (QCM) was performed by CHI400C electrochemical workstation (Shanghai Chenhua, China) at an open circuit. The gold disk electrode was pre-deposited with zinc to be as the working electrode; the platinum mesh was the counter electrode; the Ag/AgCl electrode was the reference electrode. Open circuit potential- time (OCPT) was measured with zinc foil as the working electrode, platinum mesh as the counter electrode, and Hg/Hg_2Cl_2 as the reference electrode. For the Zn//Zn Symmetric Cells, the cycling stability was investigated in a galvanostatic method conducted via the Neware battery testing system at 30 °C. Cycling behavior under different current densities (1, 5 $mA \cdot cm^{-2}$, 1 $mAh \cdot cm^{-2}$) was studied. For the $Zn//NaV_3O_8 \cdot 1.5H_2O$ and $Zn//MnO_2$ full cells, the galvanostatic method was still employed to test their cycling stability but with different current densities (1 $A \cdot g^{-1}$ and 5 $A \cdot g^{-1}$). The I-t curves, cyclic voltammetry (CV) and EIS curves were obtained by the Metrohm Autolab at 0.07 V and 0.08 V. The CV curves were measured in Zn//stainless steel (SS) configuration from −0.4 to 0.1 V and in Zn//Zn symmetric cells from 0.1 to 0.1 V at a scanning rate of 1 $mV \cdot s^{-1}$, and in $Zn//NaV_3O_8 \cdot 1.5H_2O$ full cells from 0.3 to 1.6 V at a scanning rate of 0.5 $mV \cdot s^{-1}$. The EIS curves in Zn//Zn symmetric cells and $Zn//NaV_3O_8 \cdot 1.5H_2O$ full cells were measured between 100 kHz and 0.01 Hz.

Finite Element Method Simulations: The simulations of electric fields and electrolyte current density were performed by using COMSOL Multiphysics 5.4 based on the finite element method. Deformed geometry interfaces were applied to the anode.[2] The initial concentration of Zn^{2+} was set to 1.0 $mol \cdot L^{-1}$. The exchange current density was set to be 5.0 $A \cdot m^{-2}$. The operation voltage was 0.7626 V.[3]

Computational details: The prediction of zinc morphology was performed by BFDH model in the Morphology module of Materials Studio (version 8.0) of Accelrys Inc.[4-6] The calculation models were constructed to simulate the interaction between electrolyte and electrode. A five-layer 10*10 supercell was taken as the substrate surface. Forcite module in Materials Studio of Accelrys Inc. and a Universal force field were chosen to conduct all molecular dynamics simulations.[7] The molecular dynamics simulations were carried out under an ensemble (NVE) at 298 K with a time step of 1fs. The total simulation time was 500 ps, which was long enough to reach the equilibrium state of the electrolyte system.[8] The atomic trajectories were saved and the frame was output every 5000 steps. The electrostatic interactions and the van der Waals interactions were calculated by the summation method of atom

based with the cutoff distance of 15.5 Å. The binding energy (E_b) was calculated by the following equation:

$$E_b = E_{total} - E_{substrate} - E_{liquid}$$

E_{total}, $E_{substrate}$ and E_{liquid} represent the total energy of metal substrate combined with 1M $ZnSO_4$ or 0.5M $Ce_2(SO_4)_3$, the energy of the substrate and the energy of 1M $ZnSO_4$ or 0.5M $Ce_2(SO_4)_3$, respectively.[9]

Equations

$$E_{Red} = E^{\theta}_{Red} - \frac{RT}{zF}\ln\frac{\alpha_{Red}}{\alpha_{Ox}}$$ (Equation S1)

where E_{red} is the half-cell reduction potential at the temperature of interest; E^{Θ}_{red} is the standard half-cell reduction potential; R is the universal gas constant (8.314472 J K^{-1} mol^{-1}); T is the absolute temperature (assume T = 298.15 K in this work); z is the number of electrons transferred in the cell reaction or half-reaction; F is the Faraday constant (96485.332 C mol^{-1}), and α is the chemical activity for the relevant species (α_{Red} is the activity of the reduced form and α_{Ox} is the activity of the oxidized form).[10, 11]

$$|F| = k\frac{|Q_1 Q_2|}{d^2}$$ (Equation S2)

where Q_1 represents the quantity of charge on object 1 (in Coulombs), Q_2 represents the quantity of charge on object 2 (in Coulombs), and d represents the distance of separation between the two objects (in meters). The symbol k is a proportionality constant known as the Coulomb's law constant. The value of this constant is dependent upon the medium that the charged objects are immersed in. In the case of air, the value is approximately 9.0 x 109 N • m^2 / C^2. If the charged objects are present in water, the value of k can be reduced by as much as a factor of 80.[12]

$$\Delta f = \frac{-2f_0^2}{A\sqrt{\mu\rho}}\Delta m$$ (Equation S3)

where f_0 is the resonant frequency of the crystal's fundamental mode; A is the area of the gold disk coated onto the crystal (0.205 cm^2 for given crystal); ρ is the density of the crystal and μ is the shear modulus of quartz.[13, 14]

$$(\frac{I}{I_m})^2 = \frac{1.9542}{(t/t_m)}\{1 - exp[-1.2564(t/t_m)]\}^2$$ (Instantaneous nucleation) (Equation S4)

$$(\frac{I}{I_m})^2 = \frac{1.2254}{(t/t_m)}\{1 - exp[-2.3367(t/t_m)^2]\}^2$$ (Progressive nucleation) (Equation S5)

where I and t are the current density and time, respectively, and I_m and t_m are the maximum values of the current transients.[15]

$$r_{crit} = \frac{2\gamma V_m}{F|\eta_n|}$$ (Equation S6)

where r_{crit} is the critical nuclei radius, ϒ is the surface energy of the Zn-electrolyte interface, F is Faraday's constant, V_m is the molar volume of Zn and η_n is the nucleation overpotential.[16]

Table S1. Effective reduction potentials of Ce^{3+} and La^{3+}(vs SHE) at diverse concentrations.

Cation	E^{Θ} (V)[a]	Effective reduction potential (V)		
	1 M	0.002 M	0.02 M	0.2 M
Zn^{2+}	-0.762			
Ce^{3+}	-2.336	-2.389	-2.370	-2.350
La^{3+}	-2.379	-2.432	-2.413	-2.393

Table S2 ：The results of morphology prediction.

hkl	Multiplicity	Total facet area	% Total facet area
{1 -1 0}	6	1.37×10^{-4}	41.00759
{0 0 2}	2	6.39×10^{-3}	19.17213
{1 -1 1}	12	1.33×10^{-4}	39.82028
{1 -1 2}	12		
{2 -1 0}	6		

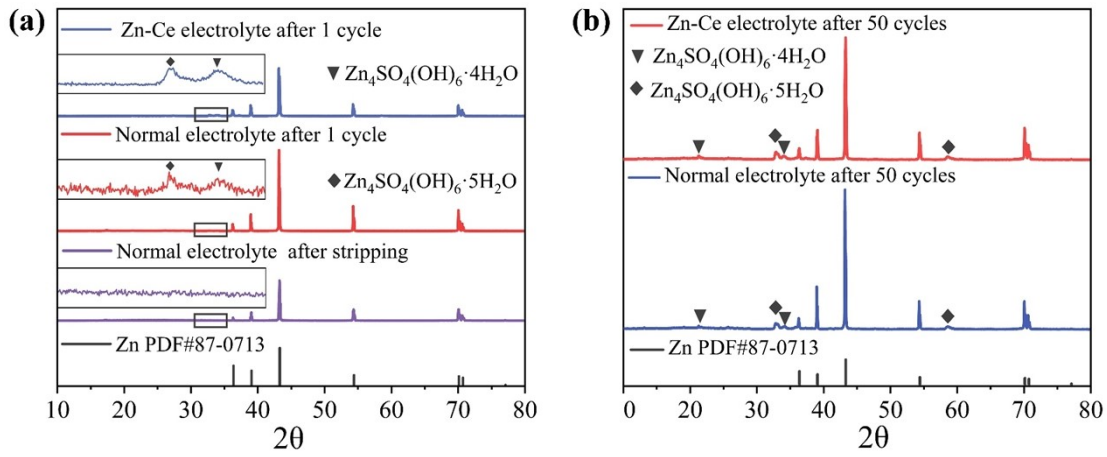

Figure S1. XRD curves of the zinc foil after 1 cycle (a) and 50 cycles (b).

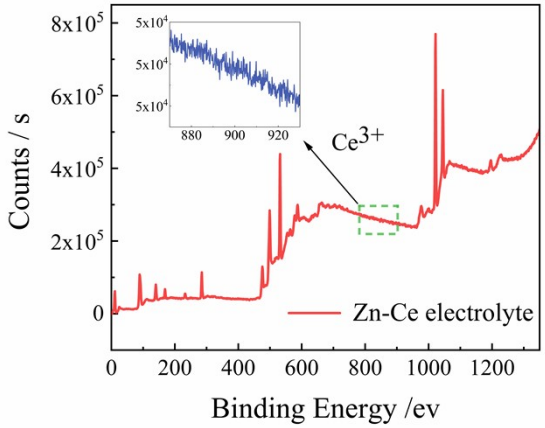

Figure S2. XPS curve of the zinc foil after 1 cycle in Zn-Ce electrolyte.

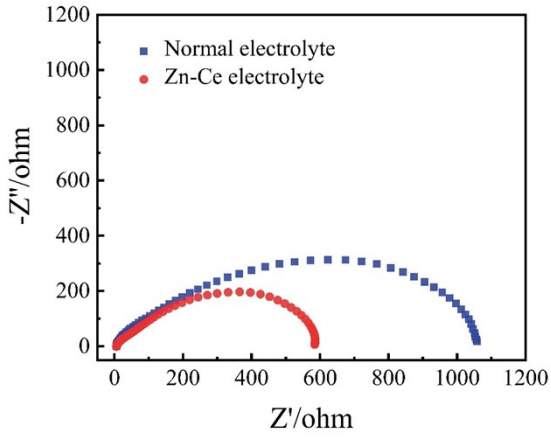

Figure S3. Electrochemical impedance spectroscopy (EIS) of the symmetric cells (vs.Zn^{2+}/Zn).

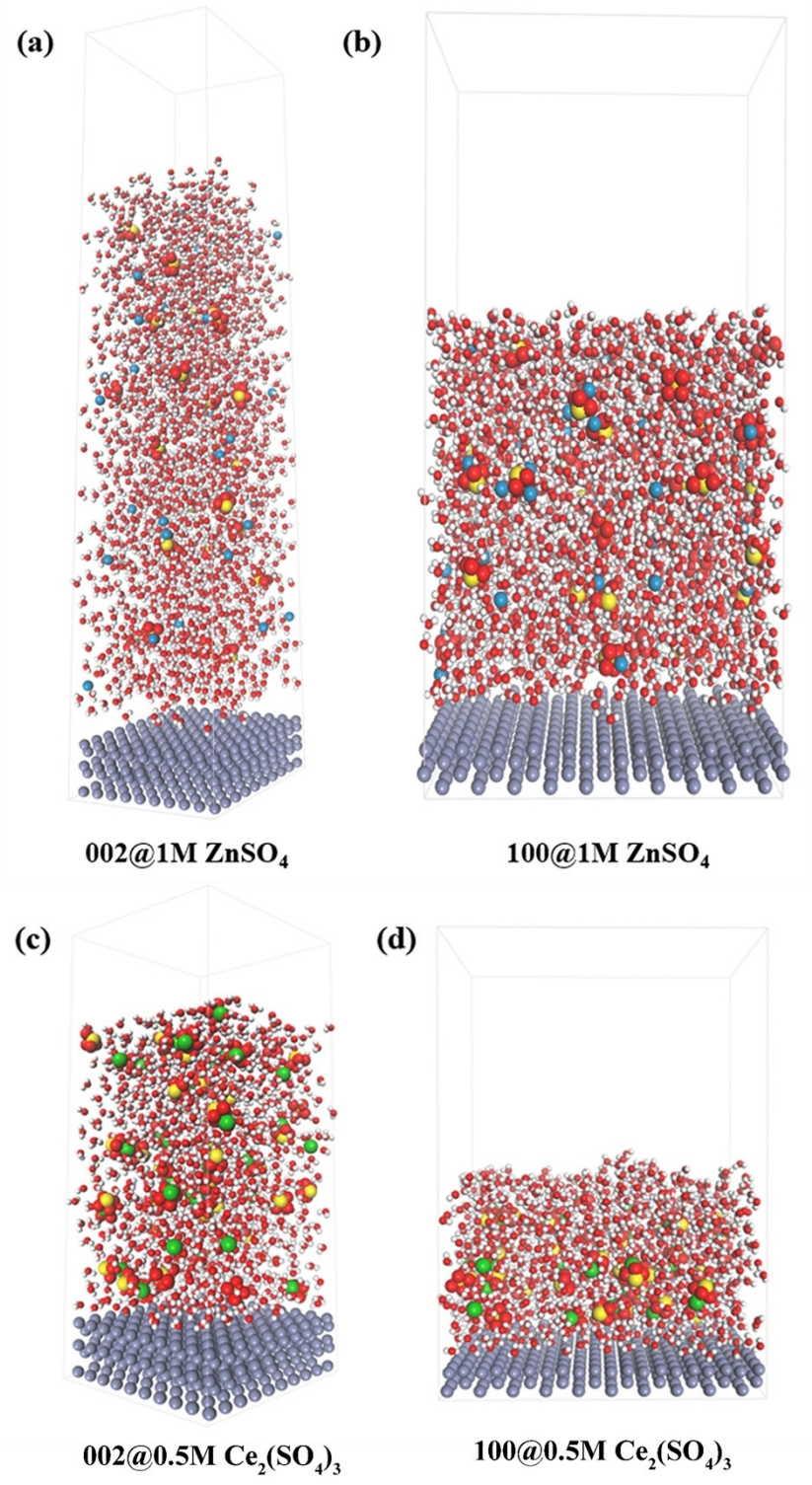

Figure S4. The calculation models of 1M $ZnSO_4$ and 0.5M $Ce_2(SO_4)_3$ interacting with (a,c) Zn 002 and (b,d) Zn 100, respectively.

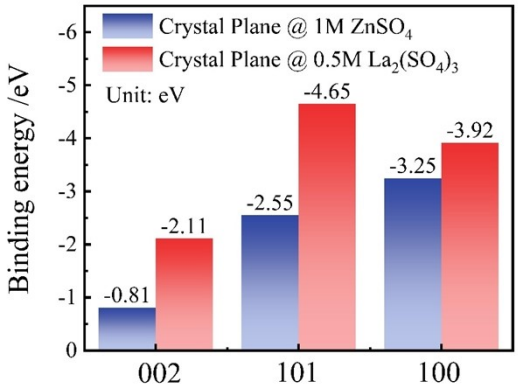

Figure S5. The binding energy of La^{3+} with different crystal planes.

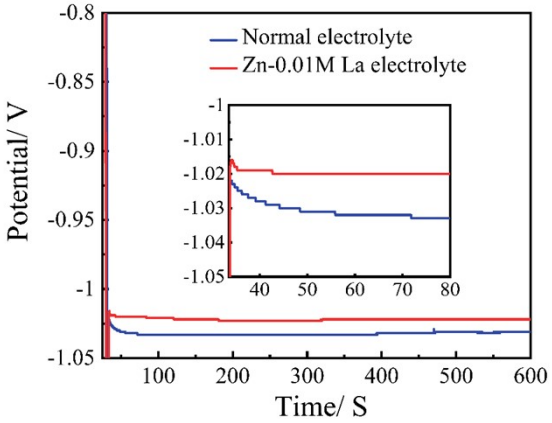

Figure S6 The curve of open circuit potential before and after getting zinc foil immersed in the electrolyte (1M $ZnSO_4$+0.01M $La_2(SO_4)_3$) (vs.SCE).

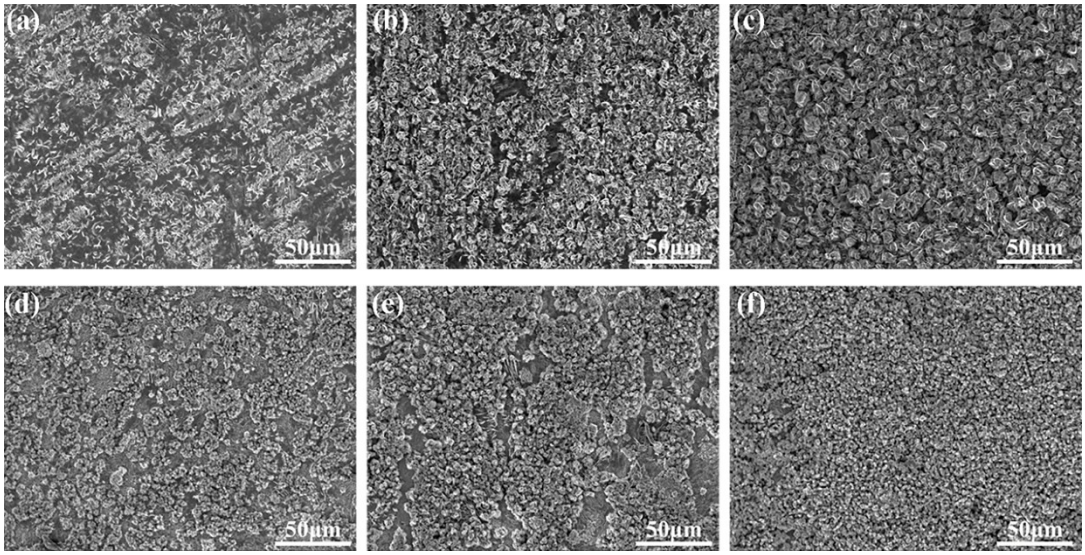

Figure S7. Morphology of the zinc anodes in (a-c) 0.01M $La_2(SO_4)_3$ electrolyte and (d-f) 0.03M $La_2(SO_4)_3$ electrolyte after deposition for 2 min, 6min and 12 min at 5 $mA \cdot cm^{-2}$, respectively.

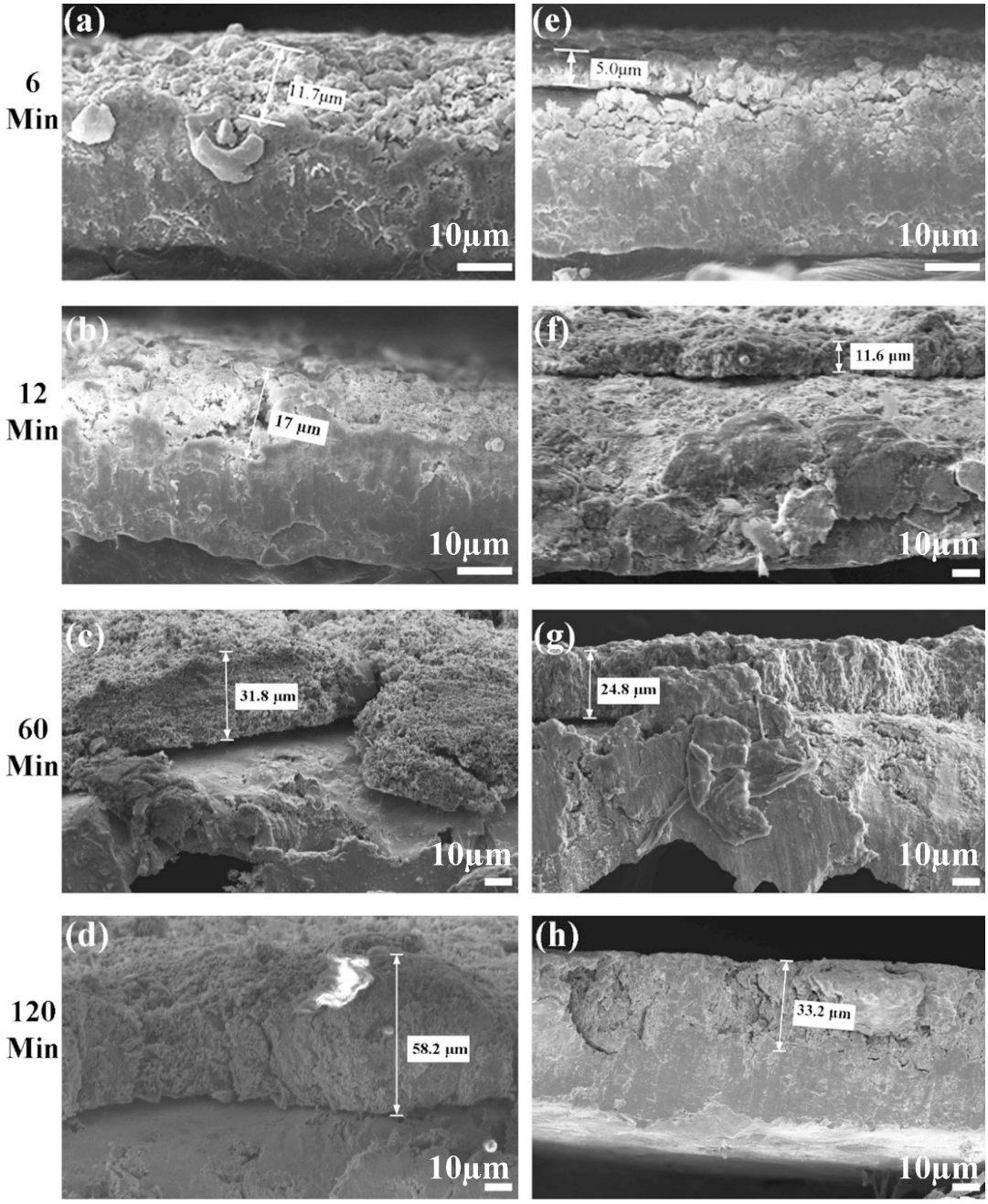

Figure S8. The cross-sectional SEM images of zinc deposition at different moments in (a-d) normal electrolytes and (e-h) Zn-Ce electrolytes.

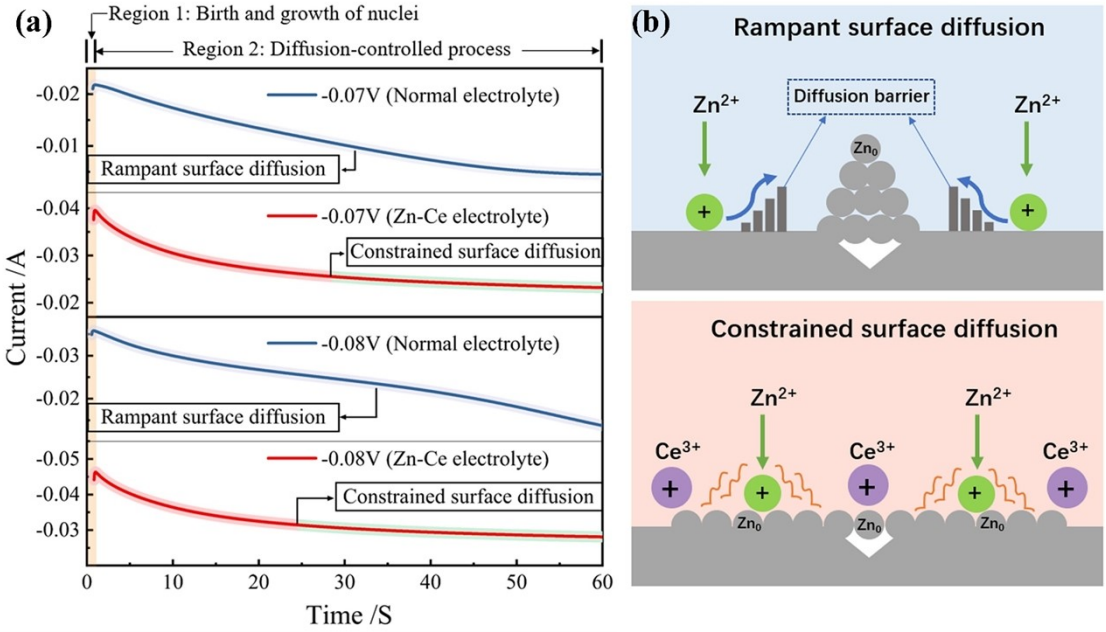

Figure S9. (a) I-t curves of symmetric cells in the normal electrolyte and Zn-Ce electrolyte (vs. Zn^{2+}/Zn). (b) Schematics of the Zn^{2+} diffusion and reduction processes in electrolytes with and without Ce^{3+}, showing that the surface diffusion is constrained in the electrolyte with Ce^{3+}.

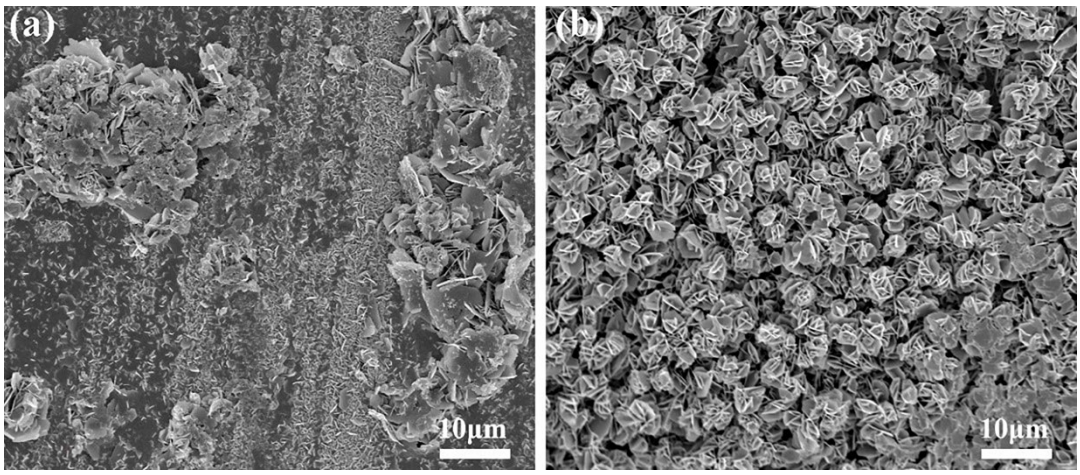

Figure S10. Morphology of the zinc anodes in (a) normal electrolyte and (b) Zn-Ce electrolyte after deposition for 12 min at 5 mA·cm^{-2}.

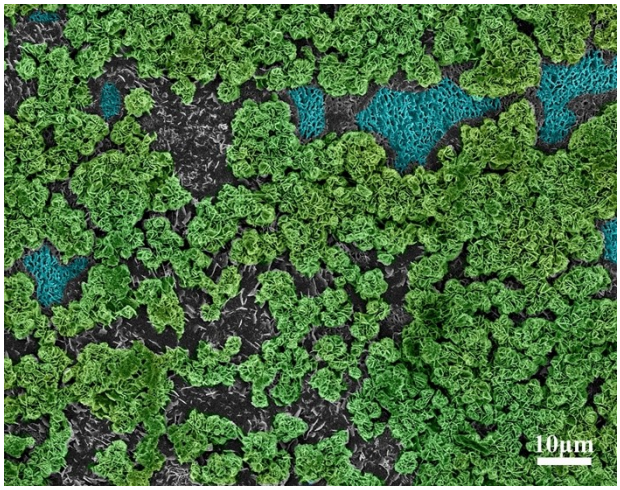

Figure S11. SEM images of the zinc anodes in Ce^{3+} electrolyte after deposition for 2 min at 5 mA·cm^{-2}.

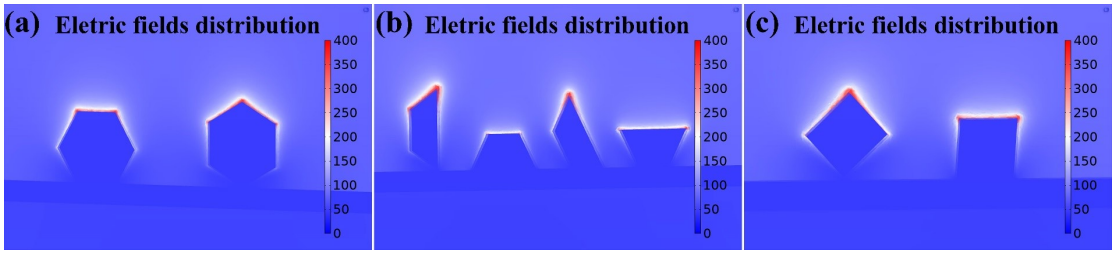

Figure S12. The distribution of electric fields for crystal planes (a) 002, (b) 101, and (c) 100 attached to zinc foil, simulated by the finite element method.

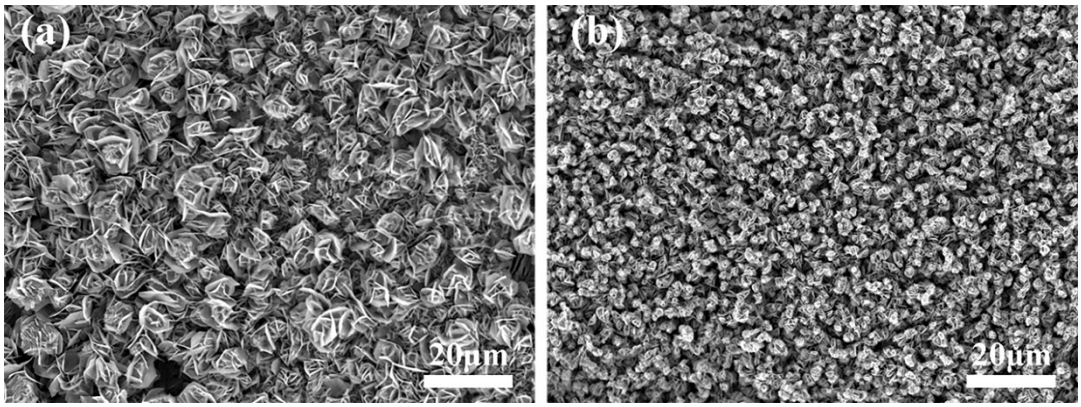

Figure S13. Morphology of the zinc anodes in (a) 0.01M $La_2(SO_4)_3$ electrolyte and (b) 0.03M $La_2(SO_4)_3$ electrolyte after deposition for 12 min at 5 mA·cm^{-2}.

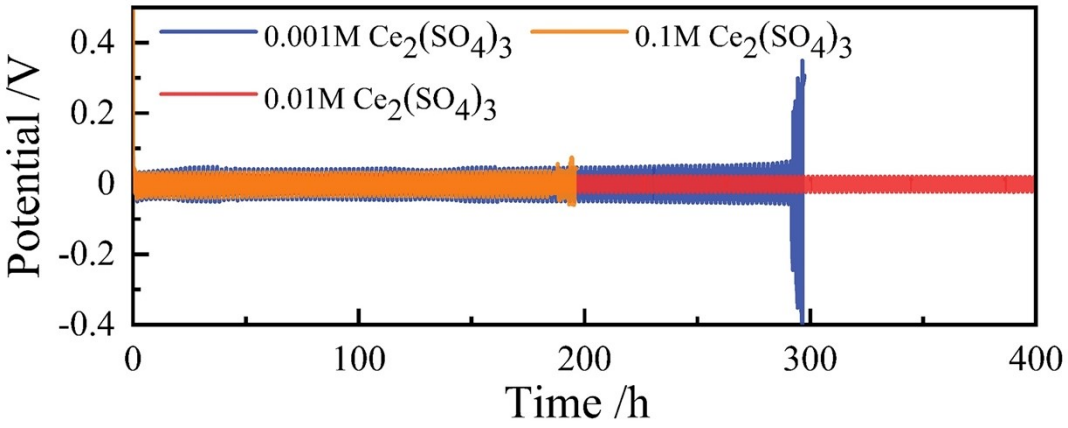

Figure S14. Cycling performance of symmetric cells in the electrolytes with different concentration of Ce^{3+} at 1 $mA \cdot cm^{-2}$ for 1 $mAh \cdot cm^{-2}$.

The extent of improvements in electrochemical performance does not positively correlate with the concentrations of Ce^{3+}. Based on the clarification of working principles of Ce^{3+} mentioned above, it makes sense that insufficient Ce^{3+} cannot fully occupy those initially active sites before deposition and dendrites still happen at unoccupied sites eventually. It is believed that Ce^{3+} can be relocated along with the change of electric fields and then those areas after Ce^{3+} removal can be exposed to zinc nucleation/growth. But some Ce^{3+} may not need to move due to the excessive amount and have to anchor themselves to their original positions.[17] In that case, the nucleation sites are very likely to be uneven and dendrites inevitably form in the end.

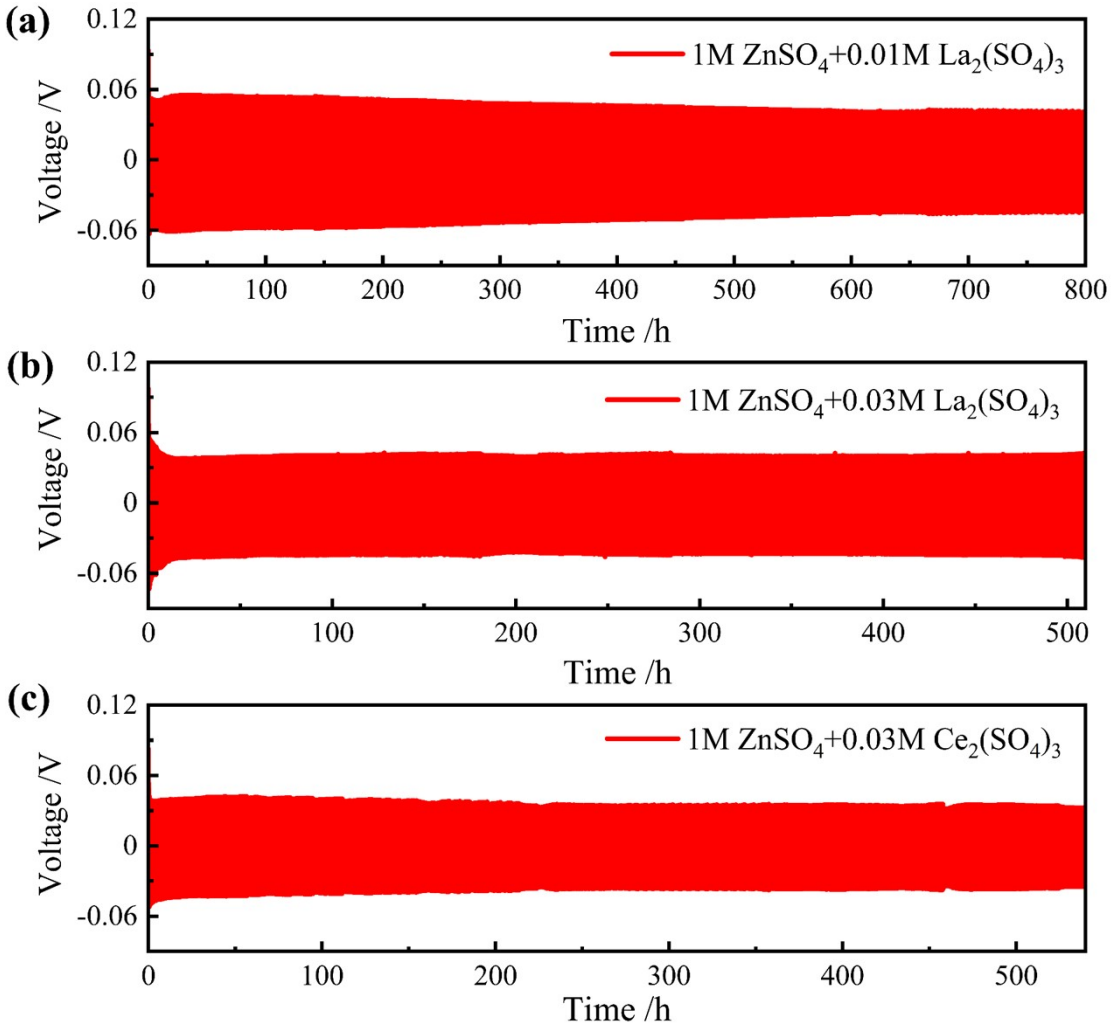

Figure S15. Cycling performance of symmetric cells in the electrolytes with 0.01M $La_2(SO_4)_3$, 0.03M $La_2(SO_4)_3$ and 0.03M $Ce_2(SO_4)_3$ at 5 mA·cm^{-2} for 1 mAh·cm^{-2}.

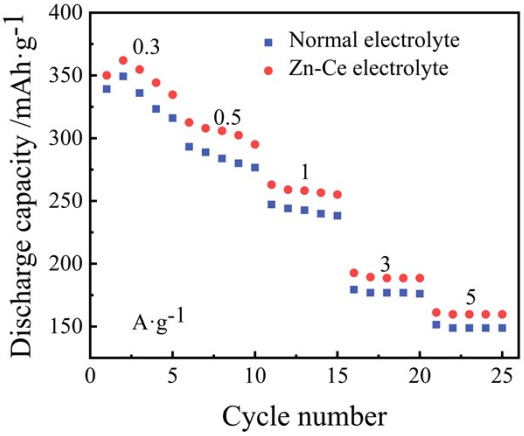

Figure S16. Rate performance of the Zn// $NaV_3O_8·1.5H_2O$ full cells using the different electrolytes at 0.3, 0.5, 1, 3 and 5 mA·g^{-1}, respectively.

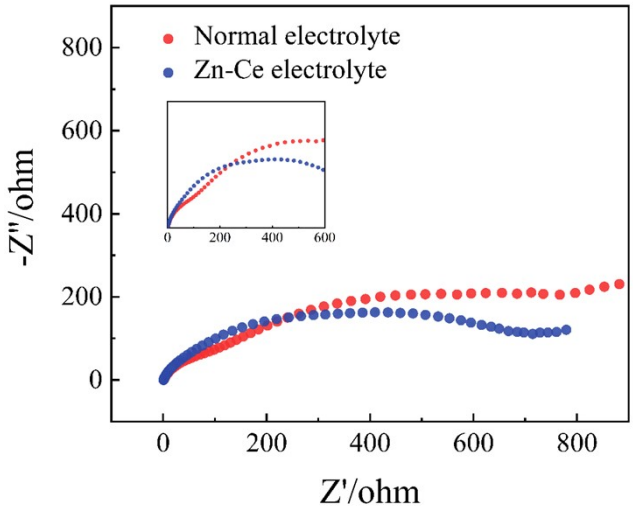

Figure S17. Electrochemical impedance spectroscopy (EIS) of the Zn//$NaV_3O_8 \cdot 1.5H_2O$ full cells.

It should be pointed out the charge transfer resistance of Zn//$NaV_3O_8 \cdot 1.5H_2O$ does not only exist at the interface between the cathode and electrolyte. It is the comprehensive results of multiple resistance which also contain the resistance of anode/electrolyte interface.

Before EIS test, the symmetric battery was rested for 8h. As demonstrated in Figure S18, cathode dissolution during that time is much more serious in the normal electrolyte than that in the Zn-Ce electrolyte. For the cathode/electrolyte interface, the decreased charge transfer resistance might benefit from the well-kept structure that allows faster Zn^{2+} insertion/extraction in Zn-Ce electrolyte whereas the destructed structure in normal electrolyte may be obstructive.

For the anode/electrolyte interface, there are two points which could support the decreased charge transfer resistance. 1. In the Zn-Ce electrolyte, the chances of receiving electrons for zinc ions could be boosted as a result of the increased nucleation sites. 2. As demonstrated in Figure S9, the surface diffusion could be constrained in the Zn-Ce electrolyte. That suggests no extra energy barrier to be overcome for zinc deposition, which contributes to the decreased charge transfer resistance.

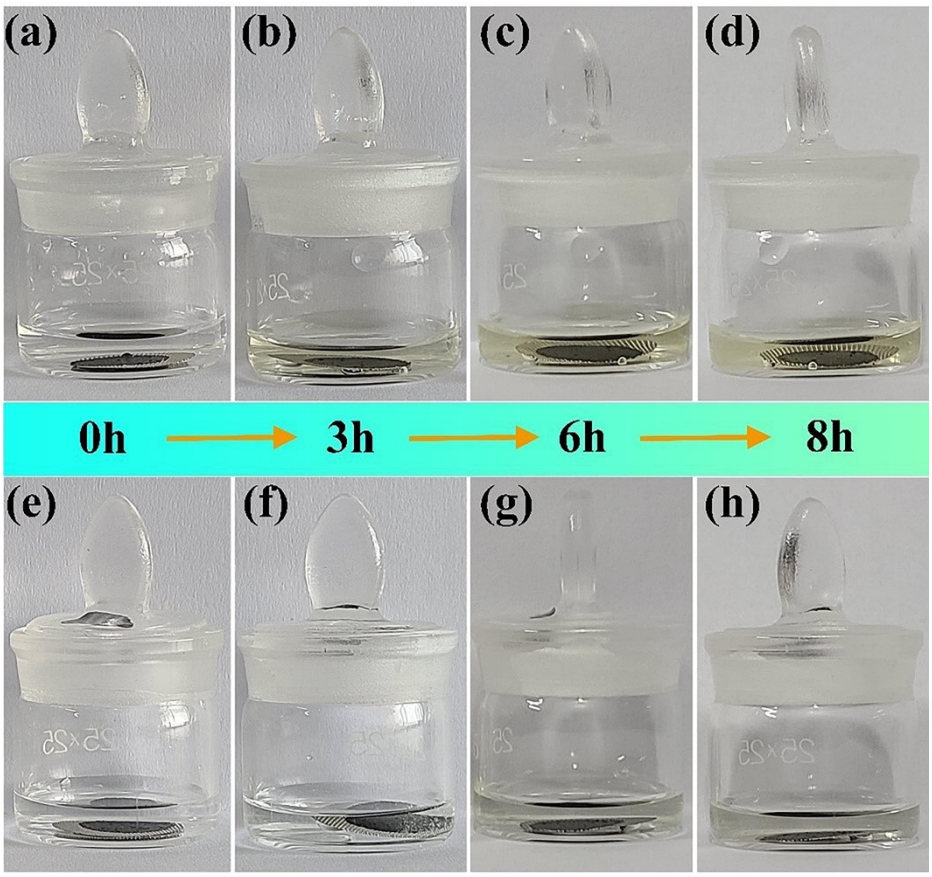

Figure S18. Color observation of the normal electrolyte (a-d) and the Zn-Ce (e-h) electrolyte with $NaV_3O_8{\cdot}1.5H_2O$ cathode immersed.

The prepared $NaV_3O_8{\cdot}1.5H_2O$ cathodes were immersed in the normal electrolyte and the Zn-Ce electrolyte for 8h, respectively. We found the normal electrolyte turns to yellow gradually whereas the Zn-Ce electrolyte still remains clear after 8h immersion, indicating the dissolution of $NaV_3O_8{\cdot}1.5H_2O$ is effectively constrained in Zn-Ce electrolyte.[1] That may give rise to the higher specific capacity in Zn-Ce electrolyte.

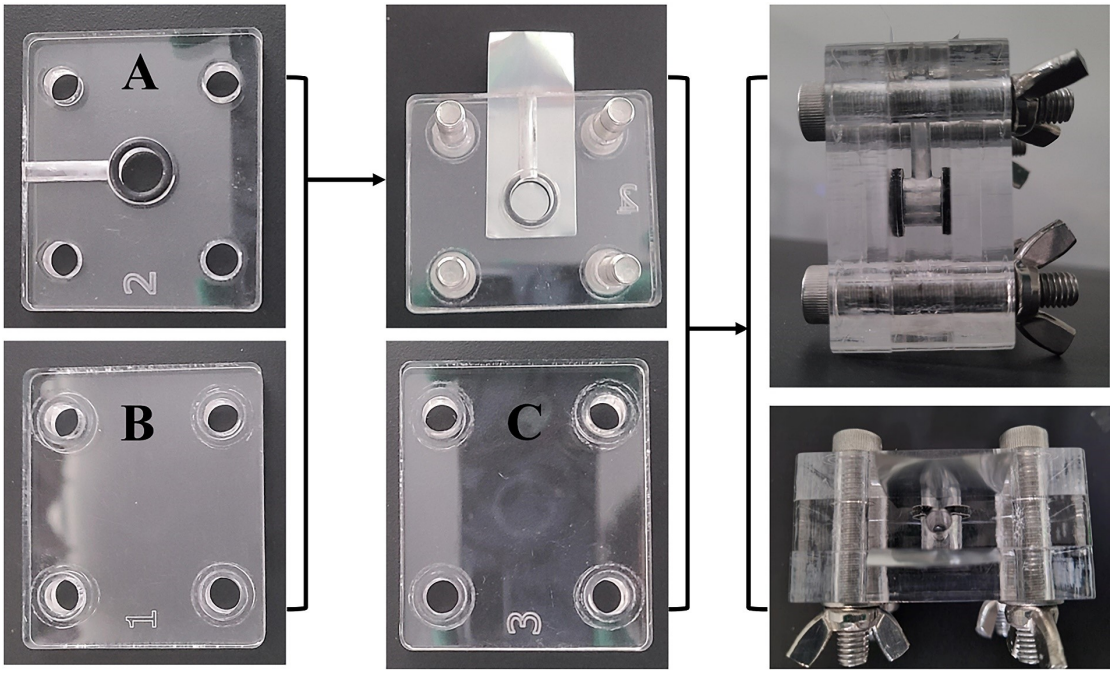

Figure S19. Pictures of the device employed to prepare SEM samples.

References

1. F. Wan, L. Zhang, X. Dai, X. Wang, Z. Niu and J. Chen, *Nat. Commun.*, 2018, **9**, 1-11.
2. X. Chen, X. Shen, T.-Z. Hou, R. Zhang, H.-J. Peng and Q. Zhang, *Chem*, 2020, **6**, 2242-2256.
3. E. Mattsson and J. M. Bockris, *Trans. Faraday Society*, 1959, **55**, 1586-1601.
4. J. D. H. Donnay and D. Harker, *American Mineralogist: Journal of Earth and Planetary Materials*, 1937, **22**, 446-467.
5. G. Friedel, *Bulletin de Minéralogie*, 1907, **30**, 326-455.
6. A. Bravais, *Études cristallographiques par M. Auguste Bravais*, Gauthier-Villars, 1866.
7. S. Chen, M. Yang, B. Liu, M. Xu, T. Zhang, B. Zhuang, D. Ding, X. Huai and H. Zhang, *RSC Adv.*, 2019, **9**, 4563-4570.
8. S. Qi, H. Wang, J. He, J. Liu, C. Cui, M. Wu, F. Li, Y. Feng and J. Ma, *Sci. Bull.*, 2021, **66**, 685-693.
9. Q. Zhang, J. Luan, L. Fu, S. Wu, Y. Tang, X. Ji and H. Wang, *Angew. Chem. Int. Ed.*, 2019, **58**, 15841-15847.
10. A. J. Bard and L. R. Faulkner, *Electrochemical Methods*, 2001, **2**, 580-632.
11. D. R. Lide, *CRC handbook of chemistry and physics*, CRC press, 2004.
12. S. Plimpton and W. Lawton, *Phys. Rev.*, 1936, **50**, 1066.
13. F. Ding, W. Xu, X. Chen, J. Zhang, Y. Shao, M. H. Engelhard, Y. Zhang, T. A. Blake, G. L. Graff and X. Liu, *J. Phys. Chem. C*, 2014, **118**, 4043-4049.
14. P. Schmutz and D. Landolt, *Electrochim. Acta*, 1999, **45**, 899-911.
15. Y. Lai, F. Liu, J. Li, Z. Zhang and Y. Liu, *J. Electroanal. Chem.*, 2010, **639**, 187-192.
16. A. Pei, G. Zheng, F. Shi, Y. Li and Y. Cui, *Nano Lett.*, 2017, **17**, 1132-1139.
17. A. Bayaguud, X. Luo, Y. Fu and C. Zhu, *ACS Energy Lett.*, 2020, **5**, 3012-3020.